Supporting Information

Synergism of Oxygen-iodine Binary Vacancies to Interfacial Electric Field: Enhancing CO_2 Photoreduction Over V_{O-I}-BiOCl/BiOI Atomic-thin Nanosheets

Juanjuan Wei,[a,b,‡] Hongliang Dong,[c,‡] Yixuan Gao,[a,‡] Xiao Su,[a] Hongwei Tan,[a] Jingjing Li,[a] Qi Zhao,[a] Xiaowen Guan,[a] Zhonglin Lu,[a] Jin Ouyang[a] and Na Na*[a]

a Key Laboratory of Radiopharmaceuticals, Ministry of Education, College of Chemistry, Beijing Normal University, Beijing 100875, China.

b College of Chemistry and Chemical Engineering, Ningxia Normal University, Guyuan 756000, China.

c Center for High Pressure Science and Technology Advanced Research, Shanghai 201203, China.

‡ These authors contributed equally to this work.

*Corresponding Author: nana@bnu.edu.cn.

Table of Contents

Experimental Procedures

Reagents:

Bismuth chloride ($BiCl_3$, 98%, Macklin), Bismuth iodide (BiI_3, >98%, TCI), Potassium iodide (KI, 98.5%, Innochem), Acetone (AR, Innochem) were purchased from commercial suppliers and used without further purification unless specified. Ultrapure water (Mill-Q, Millipore, 18.2 MΩ) was used in all experiments. All chemical reagents were in analytical grade without further purification.

Synthesis of BiOCl, BiOI, V_O-BiOCl/BiOI, V_I-BiOCl/BiOI, and $V_{O\text{-}I}$-BiOCl/BiOI 2D ultrathin nanosheets photocatalyst

The synthesis of three photocatalysts with BiOCl, BiOI and V_O-BiOCl/BiOI were achieved by one-step electrospray (ESI) microdroplet synthesis. As shown in Scheme 1, 1.0 mmol of $BiCl_3$, BiI_3, $BiCl_3$ and KI were dissolved into acetone solution in a 10 mL centrifuge tube, respectively, whose flow rate was tuned by the fluxion mixture of N_2 and O_2 (160 mL min^{-1}). The reaction was applied with a DC voltage of 20kV. Therefore, the sprayed electropositive droplets containing BiOCl, BiOI and VO-BiOCl/BiOI products were collected by a conical flask receptor attached to a negative electrode. Subsequently, the thin film BiOCl, BiOI and V_O-BiOCl/BiOI on the receptors were then dispersed in ultrapure water, respectively. Then, the mixtures were centrifuged under 12000 rpm for 15 min to obtain precipitate, which dried in a vacuum oven at 60 °C for 6 h. Finally, $V_{O\text{-}I}$-BiOCl/BiOI was prepared via heating the dry powder of V_O-BiOCl/BiOI in a muffle furnace at 140 °C for 2 h in air atmosphere. The unitary iodine vacancies of BiOCl/BiOI (V_I-BiOCl/BiOI) heterojunction was synthesized by the ESI in sufficient oxygen, which followed by the thermodynamic annealing in nitrogen atmosphere (140 °C for 2 h).

Characterization

The high voltage was supplied by a DC high-voltage power supply (China, HB-Z303-1AC). The morphology of the samples was observed with a field-emission scanning electron microscope on a voltage of 15 kV (SEM, SU-8010, Hitachi), and the transmission electron microscopy (TEM) images of all samples were recorded by a FEI Talos 200 s with an operating voltage of 200 kV (Thermo Fisher Scientific). Atomic force microscopy (AFM) and Kevin probe force microscopy (KPFM) were performed with an Asylum Research MFP-3D-BIO AFM instrument. The powder X-ray diffraction (XRD) pattern was performed with a Maxima XRD-7000 (Shimadzu, Japan). Electron paramagnetic resonance (EPR) spectra were carried out on a Bruker EMX EPR Spectrometer (Billerica, MA). Positron annihilation (PAL) of the samples were analyzed on a DPLS3000. Raman spectra was detected at room temperature using the Raman spectrometer (Renishaw RM-1000) in a back-scattering geometry with a 633 nm laser as the excitation source. The XPS spectra was conducted on a PHI-5300 ESCA spectrometer (Perkin Elmer) equipped with an Al Kα work as excitation source. The binding energies obtained in the XPS spectral analysis were corrected for specimen charging by referencing C 1s to 284.8 eV. The steady photoluminescence (PL) was performed on a steady-state fluorescence spectrophotometer (FLS980, Edinburgh Instruments). UV-vis diffuse reflectance spectroscopy (DRS) was recorded on a PerkinElmer Lambda950 spectrophotometer. *In situ* FTIR spectra were acquired from Bruker INVENIO R. Temperature-programmed desorption (TPD) spectroscopy was performed by using a AutoChem1 II 2920 with a thermal conductivity detector (TCD). The photocurrent and electrochemical impedance spectra (EIS) were measured on an electrochemical workstation (CHI 660E). 1H NMR measurement was characterized by the superconducting Fourier transform nuclear magnetic resonance spectrometer (Bruker Avance-600).

Synchrotron-radiation X-ray absorption fine structure spectra measurements

The synchrotron-radiation X-ray absorption fine structure spectra (XAFS) of Bi L_3-edge was collected on beamline

BL14W1 at the Shanghai Synchrotron Radiation Facility (SSRF). The soft X-ray absorption spectra (sXAS) of O *K*-edge and Cl *L*-edge was collected on the 4B9A station at Beijing Synchrotron Radiation Facility (BSRF) and National Synchrotron Radiation Laboratory (NSRL) in Hefei. The data was collected in fluorescence or transmission mode using a Lytle detector. The acquired extended X-ray absorption fine structure (EXAFS) data was processed according to the standard procedures using the Athena module.

The EXAFS spectra were obtained by subtracting the post-edge background from the overall absorption and then normalizing with respect to the edge-jump step. Subsequently, the χ(k) data was Fourier transformed to real (R) space to separate the EXAFS contributions from different coordination shells. To obtain the quantitative structural parameters around central atoms, least-squares curve parameter fitting was performed using the Artemis module. The following EXAFS equation was used for the calculation of the theoretical scattering amplitudes, phase shifts and the photoelectron mean free paths.

$$\chi(k)=\sum_j \frac{N_j S_o^2 F_j(k)}{kR_j^2} exp\left[-2k^2\sigma_j^2\right] exp\left[\frac{-2R_j}{\lambda(k)}\right] \sin\left[2kR_j+\Phi_j(k)\right] \quad (S\text{-}1)$$

R_j is the distance between the X-ray absorbing central atom and the atoms in the j^{th} atomic shell (backscatterer), N_j is the number of neighbors in the j^{th} atomic shell, S_0^2 is the amplitude reduction factor, $F_j(k)$ is the effective curved-wave backscattering amplitude, λ is the mean free path in Å, $\phi_j(k)$ is the phase shift (including the phase shift for each shell and the total central atom phase shift), σ_j is the Debye-Waller parameter of the j^{th} atomic shell (variation of distances around the average R_j). The functions $F_j(k)$, λ and $\phi_j(k)$ were calculated with the ab initio code FEFF9. The additional details for EXAFS simulations are given below. All fits were performed in the *R* space with *k*-weight of 3 for Bi L_3-edge. The coordination numbers of model samples were fixed as the nominal values. The obtained S_0^2 was fixed in the subsequent fitting, which made the internal atomic distances R, the Debye-Waller factor σ^2 and the edge-energy shift ΔE^0 run freely.

Photocatalytic CO_2 reduction

The photocatalytic CO_2 reduction reaction (CO_2RR) performances of the photocatalysts were carried out in a 100 mL stainless-steel photocatalytic reactor with a quartz glass lid under illumination. A 300 W Xe lamp (Beijing China Education Au-light Co., Ltd) was utilized as a light source, whose power density was about 100 mW/cm^2 with a visible-light radiometer. 15 mg photocatalyst was suspended in 20 mL of ultrapure water under magnetic stirring in the dark. The setup was initially vacuum-treated three times and then pumped with high-purity CO_2 gas (99.999%) to reach atmospheric pressure. During light irradiation, the photocatalytic reaction was typically performed for 1 h to calculate the average rates for gas production. The amounts of CO and CH_4 evolved were detected using gas chromatograph (GC, 2014C, Ar carrier, Shimadzu). The CO was converted to CH_4 though a methanation reactor and then detected by the FID. The CH_4 was conducted by a flame ionization detector (FID). Other gas products such as O_2 were monitored by a thermal conductivity detector (TCD). All gas products were injected by sampler with 1 mL gas. The isotope labeled experiments were performed using $^{13}CO_2$ instead of $^{12}CO_2$, and the products were analyzed by gas chromatography-mass spectrometry (GC-MS, 7890A, Agilent). The liquid product was analyzed by nuclear magnetic resonance spectroscopy (NMR, Bruker Avance-600), in which dimethyl sulfoxide (DMSO, Sigma, 99.99%) was used as the internal standard. The temperatures of the solutions were controlled at 298±0.2 K by a recirculating cooling water system during irradiation.

Density functional theory (DFT) calculations

All spin-polarized DFT calculations has been performed by the Vienna Ab Initio Simulation Package (VASP, version 5.4.4) with the dispersion correction (DFT+D3). The interaction between core and valence electrons was described projected augmented wave (PAW) method. The energy cutoff was set to 450 eV for the plane-wave basis

sets The Perdew-Burke-Ernzerhof (PBE) functional within the generalized gradient approximation (GGA) was employed to describe the electronic exchange correlation interaction.

Based on the vacancy concentration obtained from the experiments, a model containing 90 atoms was established (27 Bi, 27 I and 36 O atoms). Several defected models were further built based on it. First, an intrinsic oxygen vacancy was established to ensure CO_2 adsorption, named V_O-BiOI model. To investigate the influence of the iodine vacancy concentration on the reaction efficiency, three models, V_I-BiOI, $V_{O\text{-}I}$-BiOI and $V_{O\text{-}I\text{-}I}$-BiOI, were built by removing one or two I atoms, respectively. The atoms in the bottom layer were fixed in the process of structural optimization, while all the other atoms of the slab models were relaxed. For each of the slab model, the vacuum layer was set to 18 Å to avoid the interaction between atoms in adjacent unit cells perpendicular to the surface. A gamma-centered 2×2×1 *k*-point grid was set in the Brillouin zone, while the *k*-point grid was set to 4×4×1 for DOS calculating. The adsorption energies (E_{ad}) of CO_2 and CO were calculated by the following equation:

$$E_{ad} = E_{total} - E_{surface} - E_{CO_2/CO} \quad (S\text{-}2)$$

where E_{total} and $E_{CO_2/CO}$ are the energies of adsorption configuration and CO2 or CO, respectively.

$E_{surface}$represents the energy of (002) surface of BiOI.

The free energies of intermediate species were calculated as:

$$\Delta G = \Delta E + \Delta ZPE - T\Delta S \quad (S\text{-}3)$$

where ΔE was the energy difference between reactant and product molecules. Zero point energy (ΔZPE) and the entropy (ΔS) were calculated utilizing the vibrational energy of intermediates and gas phase molecules by VASPKIT.

The ESI-based microdroplet synthesis

In the typical ESI-based microdroplet synthesis, physical and chemical process were involved sequentially or simultaneously. For the cone-jet mode, the size of the droplets is usually determined by the following equation:

$$d = \alpha \frac{Q^a \varepsilon_0^b \rho^c}{\sigma^d \gamma^e} \quad (S\text{-}4)$$

where *d* is the droplet diameter, α is a constant determined by the permittivity of the liquid, Q is the liquid volume flow rate, ε_0 is the permittivity of the free space, ρ is the mass density of the liquid, σ is the liquid conductivity, and γ is the surface tension of the liquid. The exponents *a, b, c, d,* and *e* in Equation (S-4) are constants, which vary slightly according to different authors.

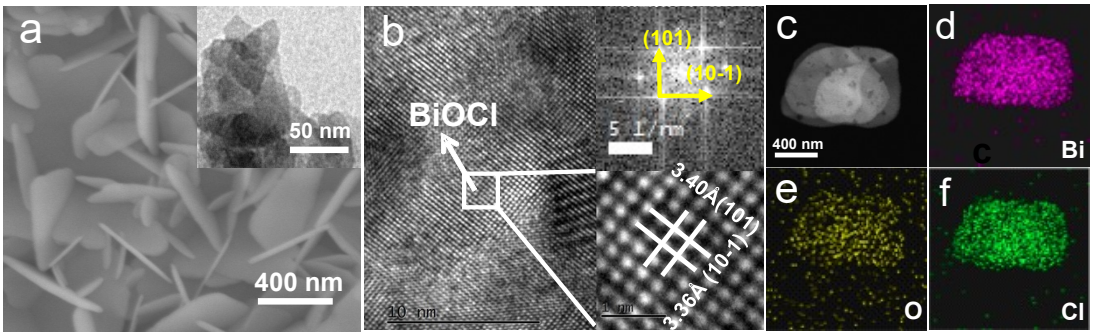

Fig. S1 The morphology characterization of BiOCl. (a) SEM and TEM (insert) images. (b) HRTEM images. Inserts: SAED patterns. (c) HAADF-STEM images. (d-f) The elemental mapping images of Bi, O, Cl in BiOCl.

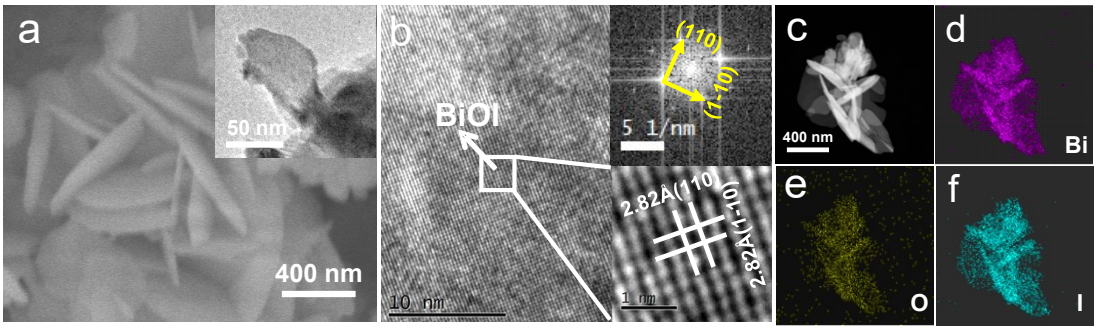

Fig. S2 The morphology characterization of BiOI. (a) SEM and TEM (insert) images. (b) HRTEM images. Inserts: SAED patterns. (c) HAADF-STEM images. (d-f) The elemental mapping images of Bi, O, I in BiOI.

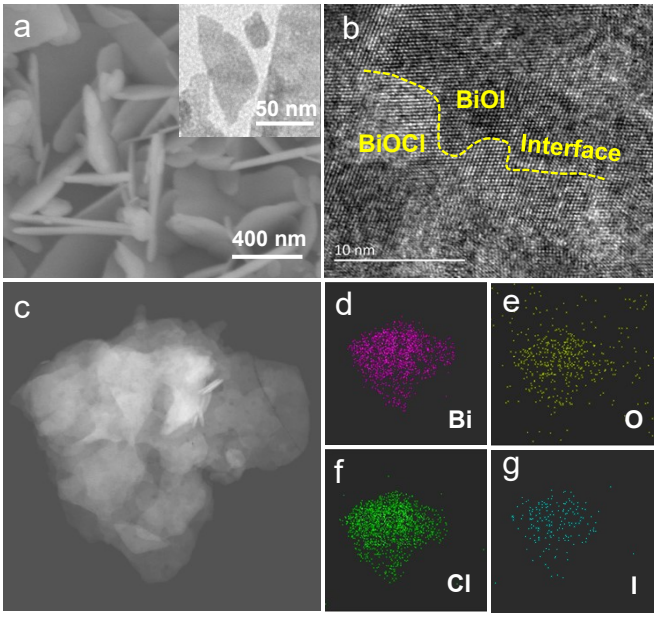

Fig. S3 The morphology characterization of V_O-BiOCl/BiOI. (a) SEM and TEM (insert) images. (b) HRTEM images. (c) HAADF-STEM images. (d-g) The elemental mapping images of Bi, O, Cl, I in V_O-BiOCl/BiOI.

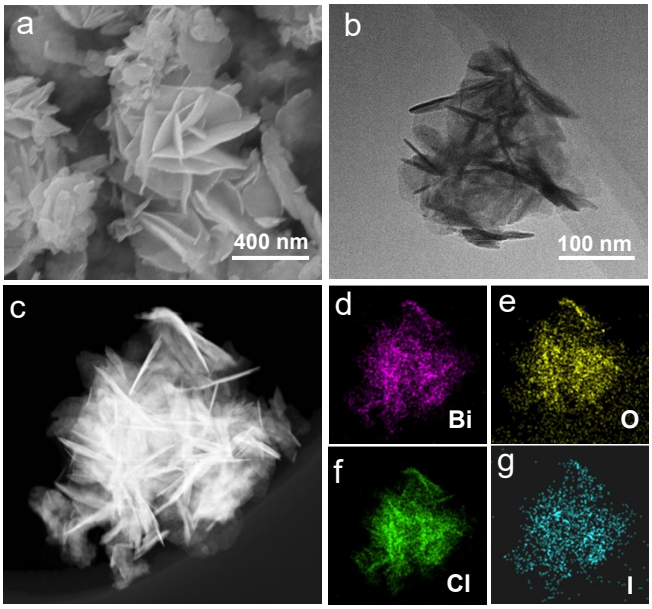

Fig. S4 The morphology characterization of V_I-BiOCl/BiOI. (a) SEM images. (b) TEM images. (c) HAADF-STEM images. (d-g) The elemental mapping images of Bi, O, Cl, I in V_I-BiOCl/BiOI.

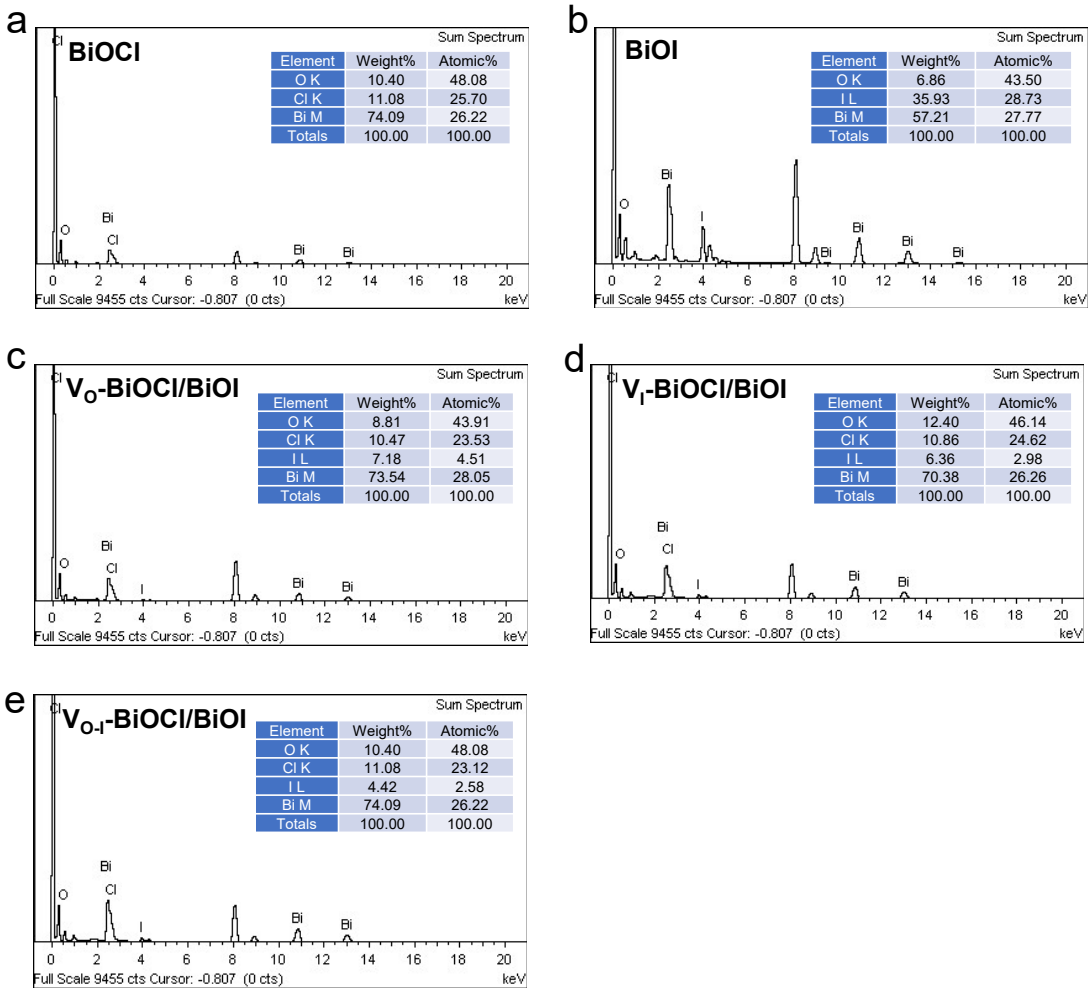

Fig. S5 The EDX spectrum for BiOCl (a), BiOI (b), V_O-BiOCl/BiOI (c), V_I-BiOCl/BiOI (d) and $V_{O\text{-}I}$-BiOCl/BiOI (e).

Table S1 The molar contents of Bi, O, I atoms in BiOI, V_O-BiOCl/BiOI, V_I-BiOCl/BiOI and V_{O-I}-BiOCl/BiOI, characterized by ICP-MS.

Photocatalyst	Bi (%)	O (%)	I (%)
BiOI	65.61	8.83	25.56
V_O-BiOCl/BiOI	70.17	8.21	14.81
V_I-BiOCl/BiOI	70.38	9.12	7.87
V_{O-I}-BiOCl/BiOI	70.29	7.07	7.61

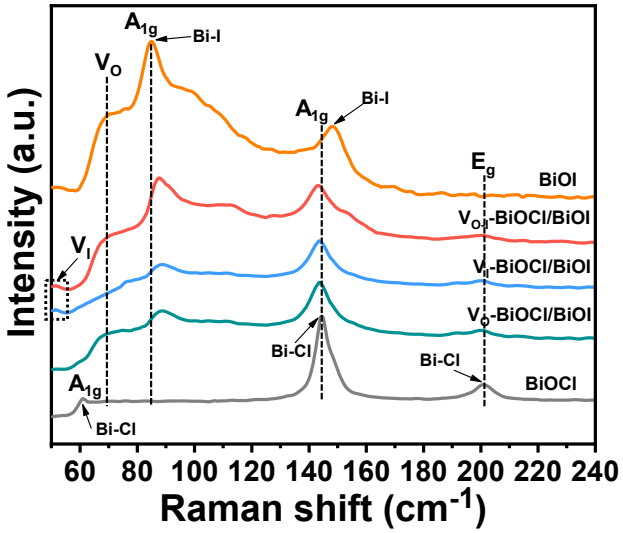

Fig. S6 The Raman spectrum for BiOCl, BiOI, V_O-BiOCl/BiOI, V_I-BiOCl/BiOI and $V_{O\text{-}I}$-BiOCl/BiOI.

Table S2 The assignments of Raman peaks for BiOCl, BiOI, V_O-BiOCl/BiOI, V_I-BiOCl/BiOI and $V_{O\text{-}I}$-BiOCl/BiOI.

Wave number (cm^{-1})	Type of the vibration
61.5, 144.4 cm^{-1}	stretching vibration of the A_{1g} external and internal Bi-Cl
200.9 cm^{-1}	stretching vibration of the E_g internal Bi-Cl
85, 148 cm^{-1}	stretching vibration of the A_{1g} external and internal Bi-I
69 cm^{-1}	stretching vibrations of oxygen vacancies
51.7 cm^{-1}	stretching vibrations of iodine vacancies

Table S3 Results of positron annihilation lifetime parameters for V_O-BiOCl/BiOI, V_I-BiOCl/BiOI and $V_{O\text{-}I}$-BiOCl/BiOI.

Sample	τ_1 (ps)	I_1 (%)	τ_2 (ps)	I_2 (%)	τ_3 (ps)	I_3 (%)
V_O-BiOCl/BiOI	227	37.8	414	57.5	2078	4.6
V_I-BiOCl/BiOI	194	10.7	467	85.7	712	3.6
$V_{O\text{-}I}$-BiOCl/BiOI	215	34.3	481	60.2	2131	5.4

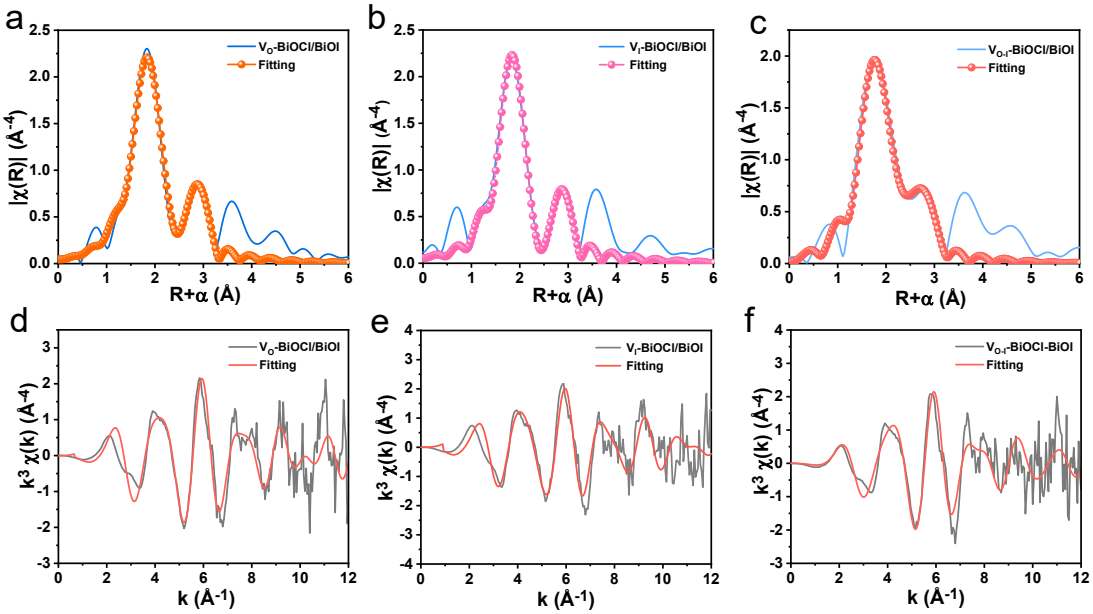

Fig. S7 The k^3-weighted EXAFS spectrum fitting of V_O-BiOCl/BiOI (a), V_I-BiOCl/BiOI (b) and V_{O-I}-BiOCl/BiOI (c). k^3 χ(k) oscillations spectra of the V_O-BiOCl/BiOI (d), V_I-BiOCl/BiOI (e) and V_{O-I}-BiOCl/BiOI (f).

Table S4 Structural parameters extracted from the Bi L_3-edge EXAFS fitting (S_0^2=0.7, determined by Bi foil standard sample).

Photocatalyst	PATH	CN	R (Å)	σ^2 (10^{-3} Å^2)	ΔE_0 (eV)	*R* factor
V_O-BiOCl/BiOI	Bi-O	3.9	2.30	9.3	1.61	0.02
	Bi-Cl	2.6	3.05	16.3		
	Bi-I	0.5	3.15	4.5		
V_I-BiOCl/BiOI	Bi-O	3.9	2.29	8.24	-3.8	0.03
	Bi-Cl	2.5	3.05	12.06		
	Bi-I	0.3	3.11	7.76		
V_{O-I}-BiOCl/BiOI	Bi-O	3.5	2.27	8.5	-3.2	0.03
	Bi-Cl	2.1	3.03	10.3		
	Bi-I	0.3	3.14	5.0		

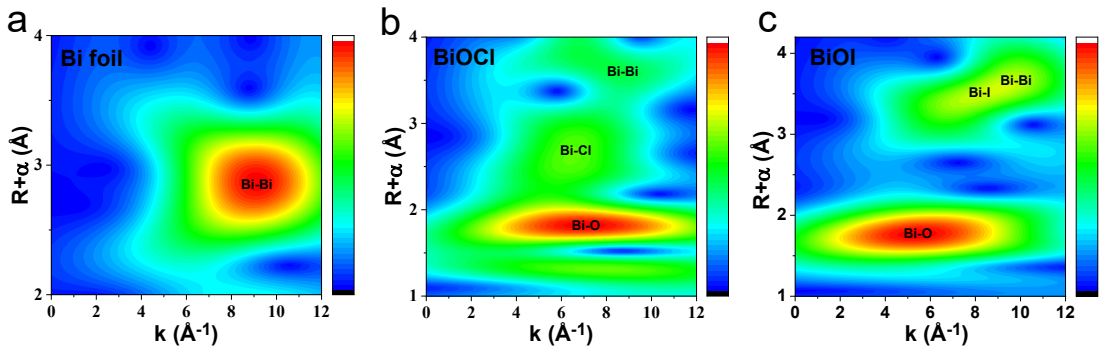

Fig. S8 Wavelet transformextended X-ray absorption fine structure (WT-EXAFS) of Bi foil (a), BiOCl (b) and BiOI (c).

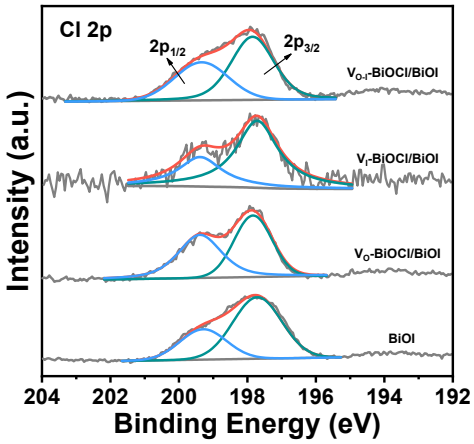

Fig. S9 XPS spectra of the Cl 2p of BiOCl, V_O-BiOCl/BiOI, V_I-BiOCl/BiOI and $V_{O\text{-}I}$-BiOCl/BiOI.

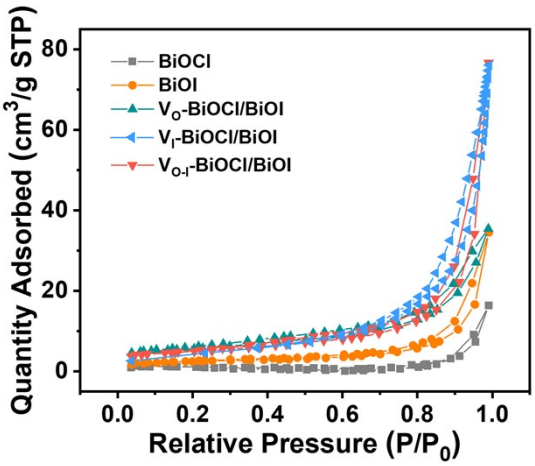

Fig. S10 N_2 sorption isotherm of photocatalysts.

Table S5 The intrinsic active sites (IAS) for the photocatalytic CO_2RR over photocatalyst.

Photocatalyst	v (CO) (μmol g^{-1} h^{-1})	SSA (m^2 g^{-1})	IAS (CO) (μmol m^{-2} h^{-1})
BiOCl	1.96	2.027	0.967
BiOI	2.56	8.883	0.288
V_O-BiOCl/BiOI	24.2	20.401	1.186
V_I-BiOCl/BiOI	50.2	19.823	2.532
V_{O-I}-BiOCl/BiOI	62.6	17.917	3.494

The intrinsic active sites (IAS) for photocatalytic CO_2RR were calculated using the following formula:

$$IAS(CO) = v(CO) / SSA_{cat} \quad (S\text{-}5)$$

where v(CO) stands for the average production rates for CO, and SSA_{cat} represents the specific surface areas of catalysts.

Table S6 Activity and selectivity for the photocatalytic reduction of CO_2 over photocatalyst.

Photocatalyst	Average production rate (μmol g^{-1} h^{-1})		Selectivity for CO production (%)
	CH_4	CO	
BiOCl	0.16	1.96	75.4%
BiOI	0.18	2.56	78.0%
V_O-BiOCl/BiOI	0.40	24.2	93.8%
V_I-BiOCl/BiOI	0.63	50.2	95.2%
$V_{O\text{-}I}$-BiOCl/BiOI	0.53	62.6	96.7%

The selectivity in hydrocarbon production was calculated based on the required electrons using the following equation:

Selectivity (%) = [2υ(CO)] / [2υ(CO) + 8υ(CH_4)] × 100% *(S-6)*

where υ(CO) and υ(CH_4) stand for the average production rates for CO and CH_4, respectively.

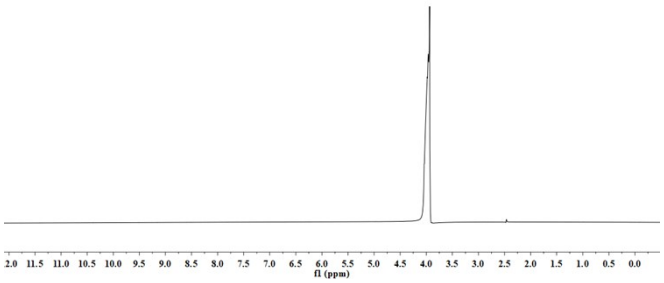

Fig. S11 Representative ^{1}HNMR spectrum of the reaction system after 10 h CO_2 photoreduction by $V_{O\text{-}I}$-BiOCl/BiOI. DMSO was used as an internal standard. The peaks at 2.45 ppm and 4.0 ppm were assigned to $(CD_3)_2SO$ and H_2O, respectively.

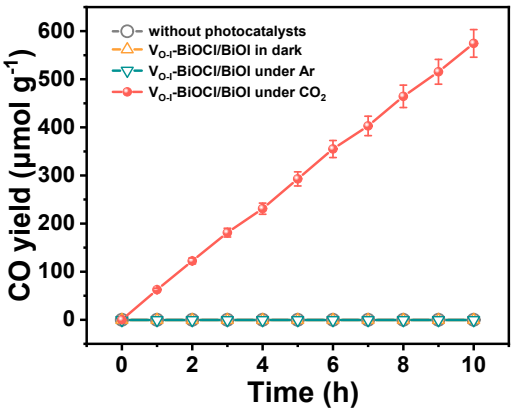

Fig. S12 Control experiments without photocatalysts, catalyzed by V_{O-I}-BiOCl/BiOI in dark or in Ar atmosphere.

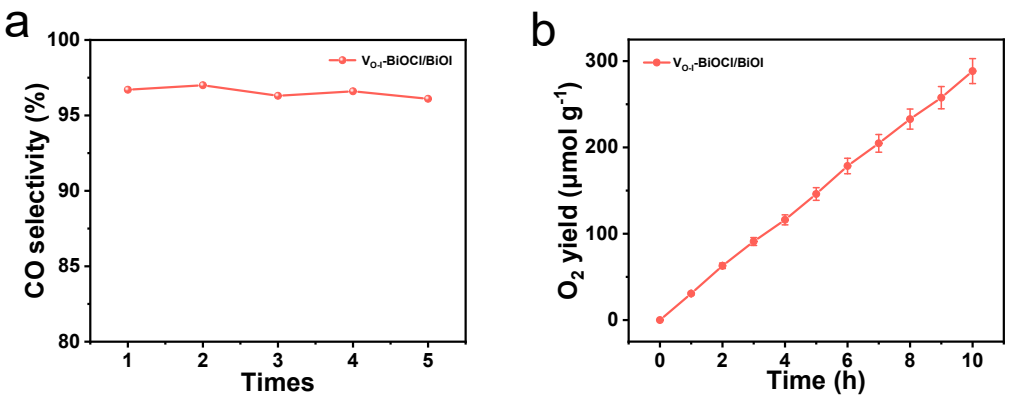

Fig. S13 (a) CO selectivity of the V_{O-I}-BiOCl/BiOI during the five cycling tests. (b) O_2 production as a function of time by V_{O-I}-BiOCl/BiOI.

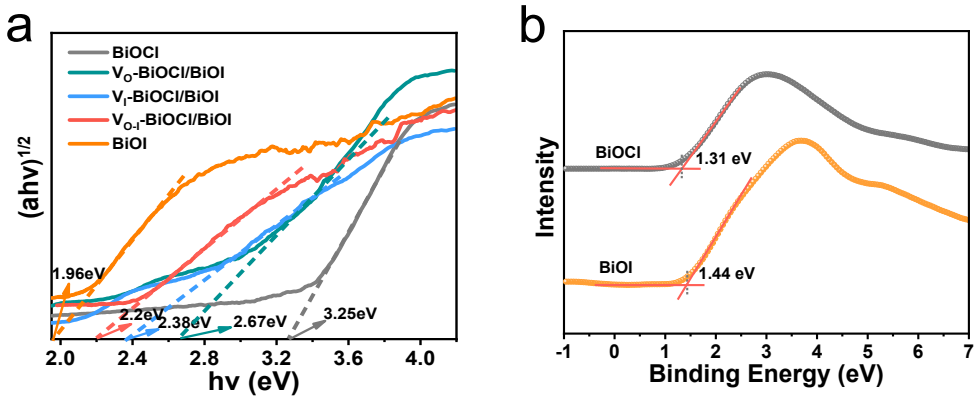

Fig. S14 (a) Bandgap spectra of BiOCl, BiOI, V_O-BiOCl/BiOI, V_I-BiOCl/BiOI and V_{O-I}-BiOCl/BiOI. (b) VBXPS spectra of BiOCl and BiOI.

The work function calculations

The work function (φ) was acquired by the contact potential difference (CPD). The CPD was measured by Kelvin Probe Force Microscope (KPFM) using highly oriented pyrolytic graphite (HOPG) as the reference. The average CPD of BiOCl, BiOI, V_O-BiOCl/BiOI, V_I-BiOCl/BiOI, $V_{O\text{-}I}$-BiOCl/BiOI and HOPG were estimated to be -407, -434, -463, -480, -486, and -395 mV from KPFM maps in Fig. 4b, and Fig. S15, respectively. The work functions (φ) can be calculated according to the following formula:

$$\varphi_{sample}\ (eV) = \varphi_{tip} + e \times CPD \qquad (S\text{-}7)$$

where φ_{tip} and φ_{sample} is the work function of the AFM tip and the sample surface, e is the charge of an electron, the work function of the HOPG is 4.6 eV. Therefore, the work functions (φ) of BiOCl and BiOI can be measured to be 4.59 and 4.56 eV.

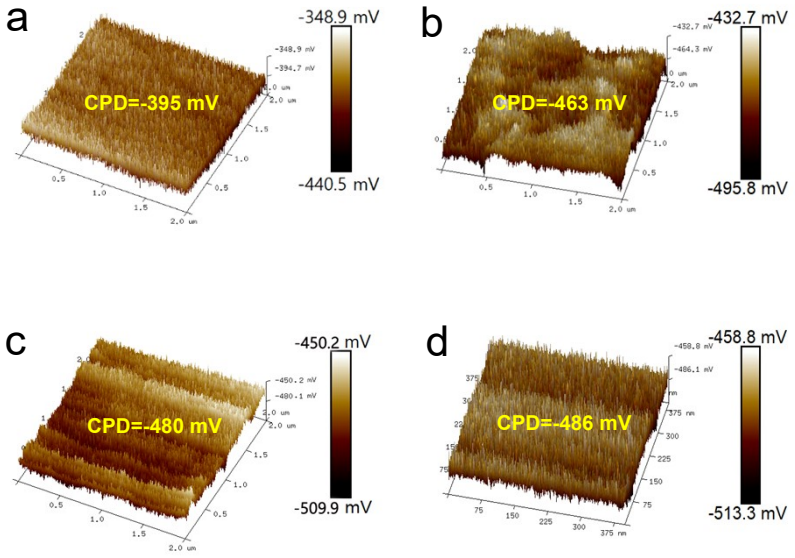

Fig. S15 The contact potential differences (CPD) measured by Kelvin probe force microscope (KPFM) for the HOPG (a), V_O-BiOCl/BiOI (b), V_I-BiOCl/BiOI (c) and $V_{O\text{-}I}$-BiOCl/BiOI (d).

The normalized time-resolved PL decay plots obtained from BiOCl, BiOI, V_O-BiOCl/BiOI, V_I-BiOCl/BiOI and $V_{O\text{-}I}$-BiOCl/BiOI can be mathematically expressed by a tri-exponential equation:

$$Fit = A+B_1 exp(-t/\tau_1) +B_2exp (-t/\tau_2) +B_3exp (-t/\tau_3) \quad (S\text{-}8)$$

where τ_1 τ_2 and τ_3 are the lifetime constants corresponding to radiative (fast) and nonradiative (slow) recombination components. A, B_1, B_2 and B_3 are constants which are obtained after fitting their decay curve, respectively. The average PL lifetime ($\tau_{average}$) were fitted by the following exponential equations:

$$\tau_{average} = (B_3\tau_3^2+B_2\tau_3^2+B_1\tau_1^2)/(B_3\tau_3+B_2\tau_3+B_1\tau_1) \quad (S\text{-}9)$$

$\tau_{average}$ reflects the overall emission decay behavior of BiOCl, BiOI, V_O-BiOCl/BiOI, V_I-BiOCl/BiOI and $V_{O\text{-}I}$-BiOCl/BiOI.

Table S7 PL Decay Parameters of the BiOCl, BiOI, V_O-BiOCl/BiOI, V_I-BiOCl/BiOI and $V_{O\text{-}I}$-BiOCl/BiOI.

Photocatalyst	τ_1(ns)	τ_2(ns)	τ_3(ns)	$\tau_{average}$ (ns)	χ
BiOCl	0.9795	3.2683	16.3085	3.7	1.014
BiOI	0.8955	2.7484	12.8277	3.3	1.142
V_O-BiOCl/BiOI	1.0896	5.1396		2.54	1.147
V_I-BiOCl/BiOI	0.8232	3.2462	24.0792	1.98	1.170
$V_{O\text{-}I}$-BiOCl/BiOI	1.1884	2.7148	15.1586	1.75	1.315

Table S8 Fitting results of impedance data of the BiOCl, BiOI, V_O-BiOCl/BiOI, V_I-BiOCl/BiOI and V_{O-I}-BiOCl/BiOI.

Photocatalyst	R_s (Ω)	R_{ct} (Ω)
BiOCl	10.34	21580
BiOI	15.1	17656
V_O-BiOCl/BiOI	10.84	11785
V_I-BiOCl/BiOI	10.56	7869
V_{O-I}-BiOCl/BiOI	10	5473

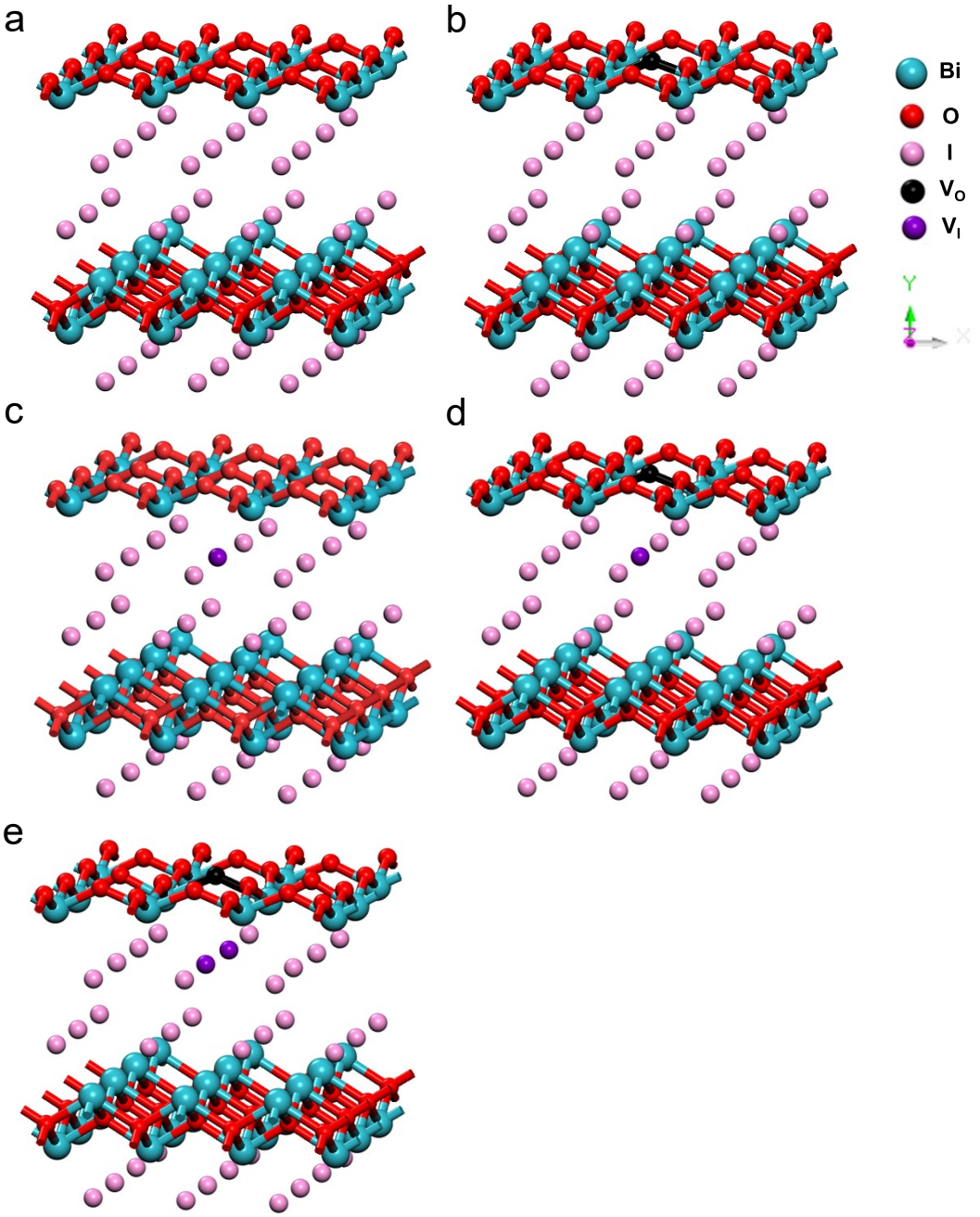

Fig. S16 The optimized structure of (a) BiOI, (b) V_O-BiOI, (c) V_I-BiOI, (d) $V_{O\text{-}I}$-BiOI and (e) $V_{O\text{-}I\text{-}I}$-BiOI.

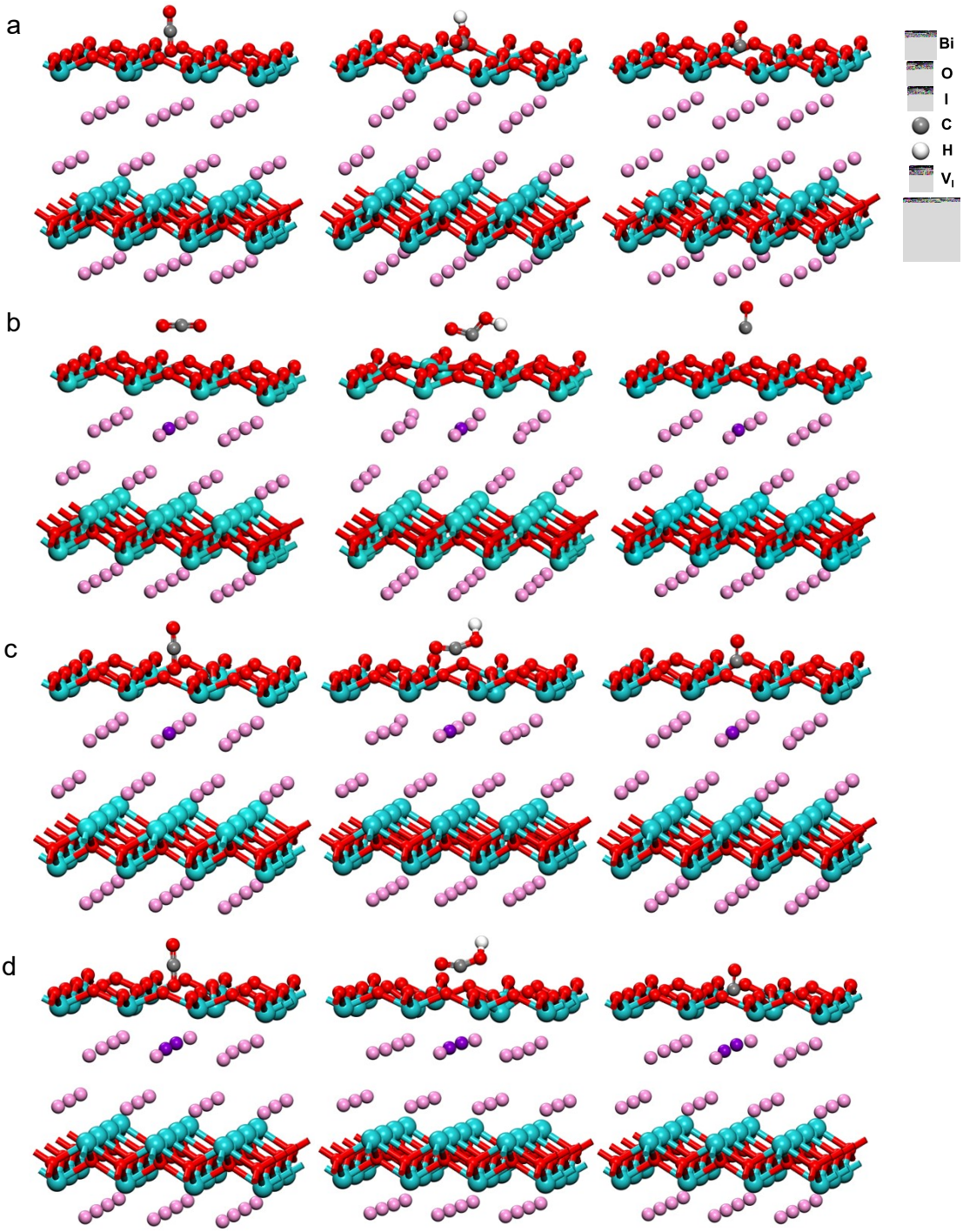

Fig. S17 The optimized structures of the stable configurations of intermediates for V_O-BiOI (a), V_I-BiOI (b), $V_{O\text{-}I}$-BiOI (c) and $V_{O\text{-}I\text{-}I}$-BiOI (d).

Table S9 Free energy barriers (ΔG) of CO_2 reduction reaction on V_O-BiOI, V_I-BiOI, $V_{O\text{-}I}$-BiOI and $V_{O\text{-}I\text{-}I}$-BiOI surface including the Zero-Point Energy Term and entropy correction. All values are in eV.

	V_O-BiOI	V_I-BiOI	$V_{O\text{-}I}$-BiOI	$V_{O\text{-}I\text{-}I}$-BiOI
$*+CO_2 \rightarrow *CO_2$	0.22	0.65	0.54	0.53
$*CO_2 + H \rightarrow *COOH$	2.52	1.89	1.55	1.20
$*COOH + H \rightarrow *CO + H_2O$	-1.92	-1.73	-1.07	-0.34
$*CO \rightarrow * + CO$	-0.11	-0.12	-0.31	-0.68

Table S10 Adsorption energy (E_{ad}) of CO_2 and CO of the V_O-BiOI, V_I-BiOI, $V_{O\text{-}I}$-BiOI and $V_{O\text{-}I\text{-}I}$-BiOI. All values are in eV.

	V_O-BiOI	V_I-BiOI	$V_{O\text{-}I}$-BiOI	$V_{O\text{-}I\text{-}I}$-BiOI
CO_2	-0.24	0.19	0.07	0.07
CO	-0.33	0.10	-0.11	0.18

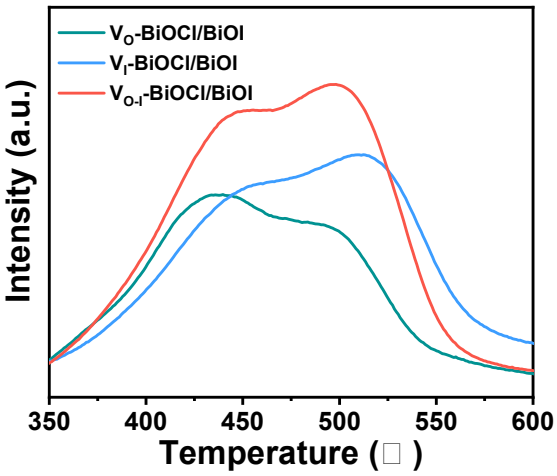

Fig. S18 CO_2-TPD profiles of V_O-BiOCl/BiOI, V_I-BiOCl/BiOI and V_{O-I}-BiOCl/BiOI.

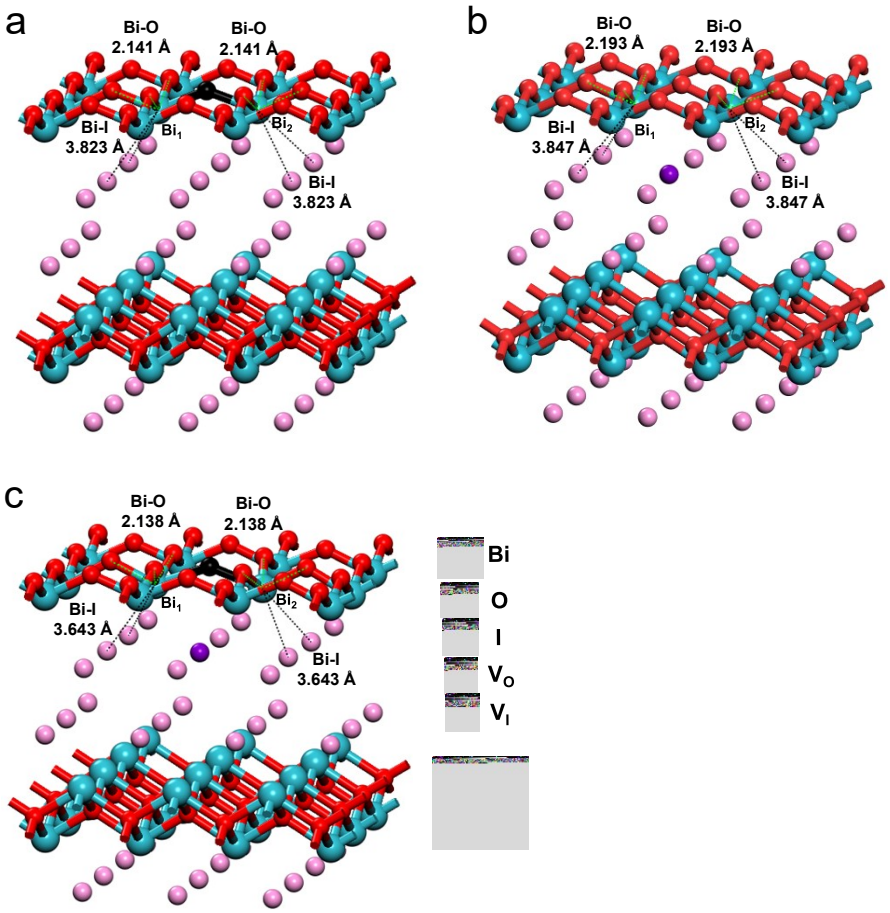

Fig. S19 Calculated bond length of the optimized structure for V_O-BiOI (a), V_I-BiOI (b) and $V_{O\text{-}I}$-BiOI (c).

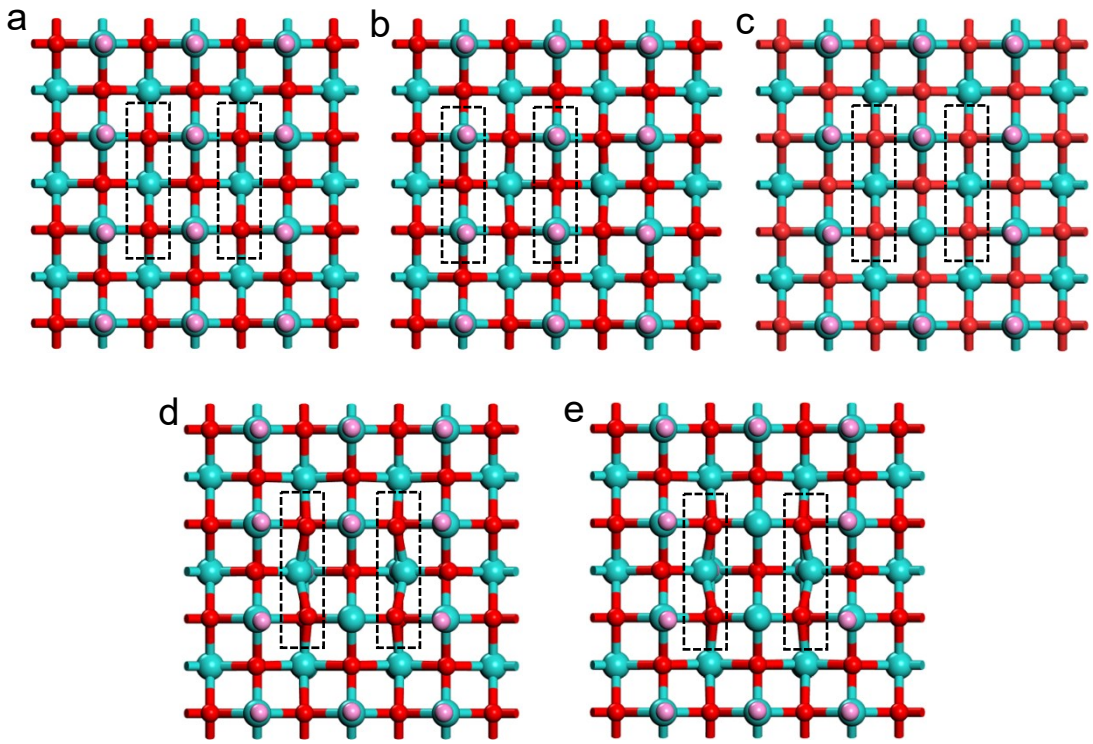

Fig. S20 The distorted structures from different vacancies for BiOI (a), V_O-BiOI (b), V_I-BiOI (c), $V_{O\text{-}I}$-BiOI (d) and $V_{O\text{-}I\text{-}I}$-BiOI (e).